Electronic supplementary materials

For https:// doi.org/10.1631/jzus.A2500007

High-performance milling of Ti-6Al-4V through rotary ultrasonic elliptical milling with anticlockwise elliptical vibration

Lianxing LIU[1,2], Xinggang JIANG[1,2], Enze YING[1,2], Zhefei SUN[1,2], Daxi GENG[1,2], Deyuan ZHANG[1,2]

[1]*School of Mechanical Engineering and Automation, Beihang University, Beijing 100191, China*

[2]*Institute of Bionic and Micro-Nano Systems, Beihang University, Beijing 100191, China*

S1: Simplified theoretical motion trajectory derivation

Based on prior research findings, the motion path of the tool tips in CRUEM can be calculated as follows (Liu et al., 2019):

$$\begin{cases} x_{\mathrm{CRUEM}} = r\sin\left(\frac{2\pi n}{60}t - \mathrm{i}\delta\right) + A\sin\left(2\pi f t + \frac{2\pi n}{60}t\right) + \frac{n v_f Z}{60}t \\ y_{\mathrm{CRUEM}} = r\cos\left(\frac{2\pi n}{60}t - \mathrm{i}\delta\right) + A\cos\left(2\pi f t + \frac{2\pi n}{60}t\right) \end{cases}. \tag{S1}$$

where r is the radius of the end mill, t is the cutting time, $\delta = 2\pi/Z$ is the angle between two adjacent tool tips, Z is the total sum of tool tips, i is the serial number of the selected tool tip, (i= 1,2, ⋯ , Z), n is the spindle speed, v_f is the feed rate of the workpiece. A is the vibration amplitude of the tool tips, and f is the vibration frequency. By reversing the direction of vibration, the motion path of tool tips in ARUEM can be calculated as:

$$\begin{cases} x_{\mathrm{ARUEM}} = r\sin\left(\frac{2\pi n}{60}t - \mathrm{i}\delta\right) + A\sin\left(2\pi f t + \frac{2\pi n}{60}t\right) + \frac{n v_f Z}{60}t \\ y_{\mathrm{ARUEM}} = r\cos\left(\frac{2\pi n}{60}t - \mathrm{i}\delta\right) - A\cos\left(2\pi f t + \frac{2\pi n}{60}t\right) \end{cases}. \tag{S2}$$

The theoretical motion trajectory in the superficial layer can be described as fluctuating forward in the X direction. This is because the surface integrity of the machined surface is primarily influenced by the movement trajectory of the cutting edges near the machined surface, while material further from the final surface will be removed during subsequent cutting passes. Additionally, the ultrasonic vibration frequency is significantly higher than the spindle rotation frequency, allowing the rotary motion of the tool tips to be approximated as translational motion. Furthermore, the feed speed of the workpiece is negligible when compared to the linear speed of spindle rotation and the speed of ultrasonic vibration. Thus, the theoretical trajectory of one tool tip in ARUEM can be simplified as

$$\begin{cases} x_{\mathrm{ARUEM}} = -\frac{2\pi n r}{60}t - A\sin(2\pi f t) \\ y_{\mathrm{ARUEM}} = A\cos(2\pi f t) \end{cases}. \tag{S3}$$

The theoretical trajectory of one tool tip in CRUEM can be simplified as:

$$\begin{cases} x_{\mathrm{CRUEM}} = -\dfrac{2\pi nr}{60}t + A\sin(2\pi ft) \\ y_{\mathrm{CRUEM}} = A\cos(2\pi ft) \end{cases}. \tag{S4}$$

S2: Cutting speed in ARUEM

The cutting speeds in ARUEM can be obtained as

$$\begin{cases} v_{AX} = -\dfrac{2\pi nr}{60} - 2\pi fA\cos(2\pi ft) \\ v_{AY} = -2\pi fA\sin(2\pi ft) \end{cases}. \tag{S5}$$

Eq. (S5) shows the cutting speeds in the *X* and *Y* directions in ARUEM, and the cutting speeds in CRUEM can be obtained in the same manner as

$$\begin{cases} v_{CX} = -\dfrac{2\pi nr}{60} + 2\pi fA\cos(2\pi ft) \\ v_{CY} = -2\pi fA\sin(2\pi ft) \end{cases}. \tag{S6}$$

The resultant speed of ARUEM and CRUEM can be calculated as:

$$\begin{cases} v_{\mathrm{ARUEM}} = \sqrt{\left(v_{AX}\right)^2 + \left(v_{AY}\right)^2} \\ v_{\mathrm{CRUEM}} = \sqrt{\left(v_{CX}\right)^2 + \left(v_{CY}\right)^2} \end{cases}. \tag{S7}$$

Previous studies have primarily focused on the time-varying characteristics of cutting speed in CRUEM as illustrated in Fig. S1a. However, the variations in cutting speed at different positions along the cutting trajectory are more critical for analysing cutting characteristics. Fig. S1b and Fig. S1c demonstrate the relationship between the resultant cutting speed and cutting trajectory in ARUEM and CRUEM, and cutting speed in conventional milling (referred to as CM, and the cutting speed in CM is referred to as v_c).

In both ARUEM and CRUEM, ultrasonic vibration causes the cutting speed of the cutting edge to periodically vary over a wide range, creating conditions for potential intermittent cutting between the cutting edge and the workpiece. The amplitude of this periodic variation depends on the vibration amplitude. When the cutting edge separates from the workpiece, cutting fluid enters the cutting zone, enhancing the machining environment. Owing to the overlapping trajectories of the four cutting edges, there are more opportunities for cutting to occur closer to the valley of the motion trajectory. At this point, the average cutting speed in CRUEM is higher than that in CM, with the maximum speed being 69% greater than in CM. In contrast, the cutting speed in ARUEM is lower than that in CM. Without thermal softening, a lower cutting speed reduces the load on the cutting edge, potentially improving the cutting quality within a unit in ARUEM.

It is important to note that, although the cutting speed increases at the valley of the cutting trajectory in CRUEM, its unit cutting quality still surpasses that of CM. This is attributed to the separation effect during the cutting process in CRUEM, which promotes heat dissipation and lubrication.

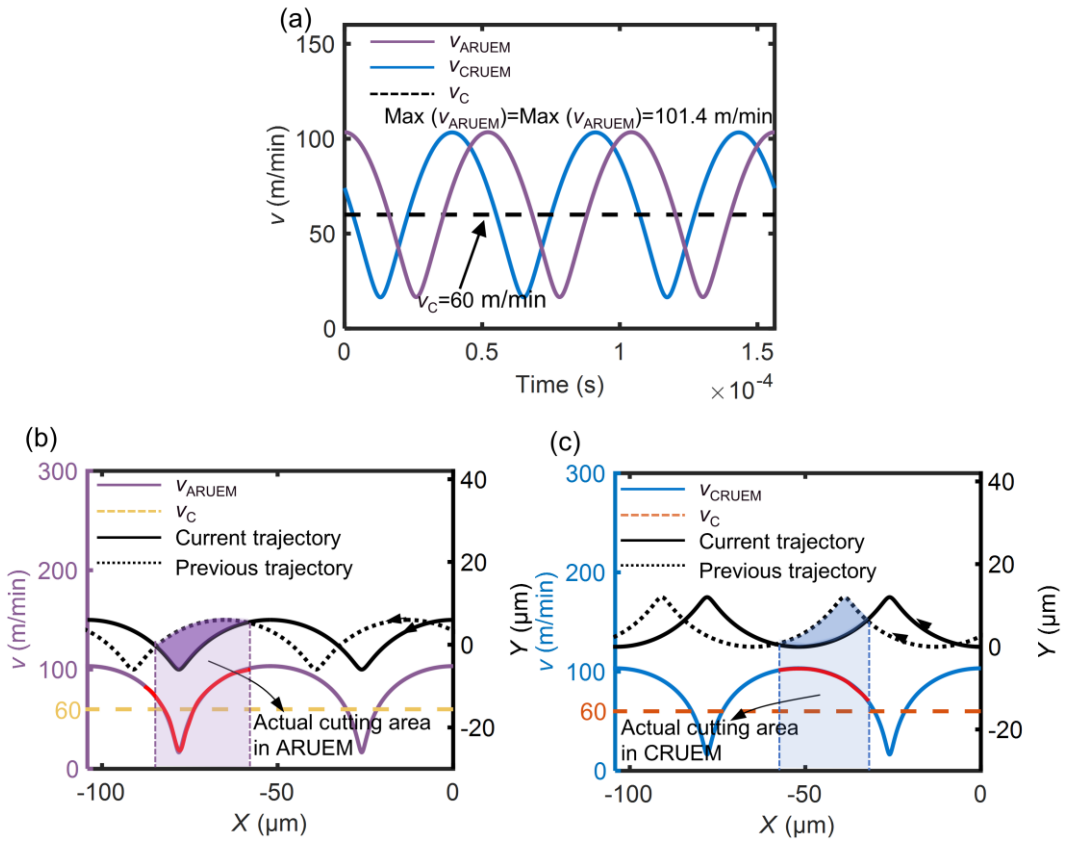

Fig. S1. Cutting speed v_c (a) varied with time, and varied with X position in (b) ARUEM and (c) CRUEM at v_c = 60 m/min, A = 6 μm and v_f = 0.015 mm

S3: Acceleration in ARUEM

The accelerations in the X and Y directions in ARUEM can be obtained as:

$$\begin{cases} a_{AX} = -(2\pi f)^2 A\sin(2\pi f t) \\ a_{AY} = (2\pi f)^2 A\cos(2\pi f t) \end{cases}. \tag{S8}$$

The accelerations in the X and Y directions in the CRUEM can be obtained similarly

$$\begin{cases} a_{CX} = -(2\pi f)^2 A\sin(2\pi f t) \\ a_{CY} = -(2\pi f)^2 A\cos(2\pi f t) \end{cases}. \tag{S9}$$

The total cutting edge acceleration in ARUEM and CRUEM can be calculated as follows:

$$\begin{cases} a_{ARUEM} = \sqrt{(a_{AX})^2 + (a_{AY})^2} \\ a_{CRUEM} = \sqrt{(a_{CX})^2 + (a_{CY})^2} \end{cases}. \tag{S10}$$

The motion of the cutting edge in ARUEM and CRUEM, as shown in Fig. S2, results from the combined effects of milling cutter rotation, ultrasonic elliptical vibration, and feed motion. Both the milling cutter rotation and ultrasonic elliptical vibration exhibit constant acceleration values directed toward the centers of their respective circular paths. As indicated in Fig. S2a, the acceleration of the cutting edge due to rotation is substantially lower than that caused by ultrasonic elliptical vibration, which is consistent with previous studies(Sun et al., 2024). This research emphasizes the acceleration induced by ultrasonic elliptical vibration, as it represents the force transmitted to the cutting edge by the vibration cutting system.

Focusing on the cutting edge as the subject of analysis, its gravitational force is negligible. When unloaded, the cutting edge is influenced mainly by the elastic force generated by the vibration cutting system, with the driving force ensuring the cutting edge attains a specific acceleration.

Given the constant magnitude of acceleration, understanding its directional characteristics at different cutting positions is crucial. Fig. S2b and Fig. S2c illustrate the accelerations in the *X* and *Y* directions for ARUEM and CRUEM at various points along the cutting trajectory. In these figures, the *X* direction acceleration is negative, reflecting the cutting edge's movement in the negative *X* direction. These visualizations facilitate comprehension of how acceleration changes at different trajectory positions.

Both ARUEM and CRUEM exhibit periodic variations in the accelerations along the *X* and *Y* directions. In ARUEM, the proportion of trajectory points where the *Y* direction acceleration is directed toward the negative *Y* axis is significantly higher than in CRUEM, suggesting a stronger cutting ability in this direction (Sun, et al., 2024). This is due to the increase in acceleration, which enhances the instantaneous impact force of the cutting edge. This may facilitate the disruption of the dislocation structure in titanium alloys, promoting crack propagation and consequently improving the cutting capability of the cutting edge. Conversely, CRUEM shows a larger negative *Y*-axis force during the cutting-in phase, which contributes to the ironing effect on the tool flank.

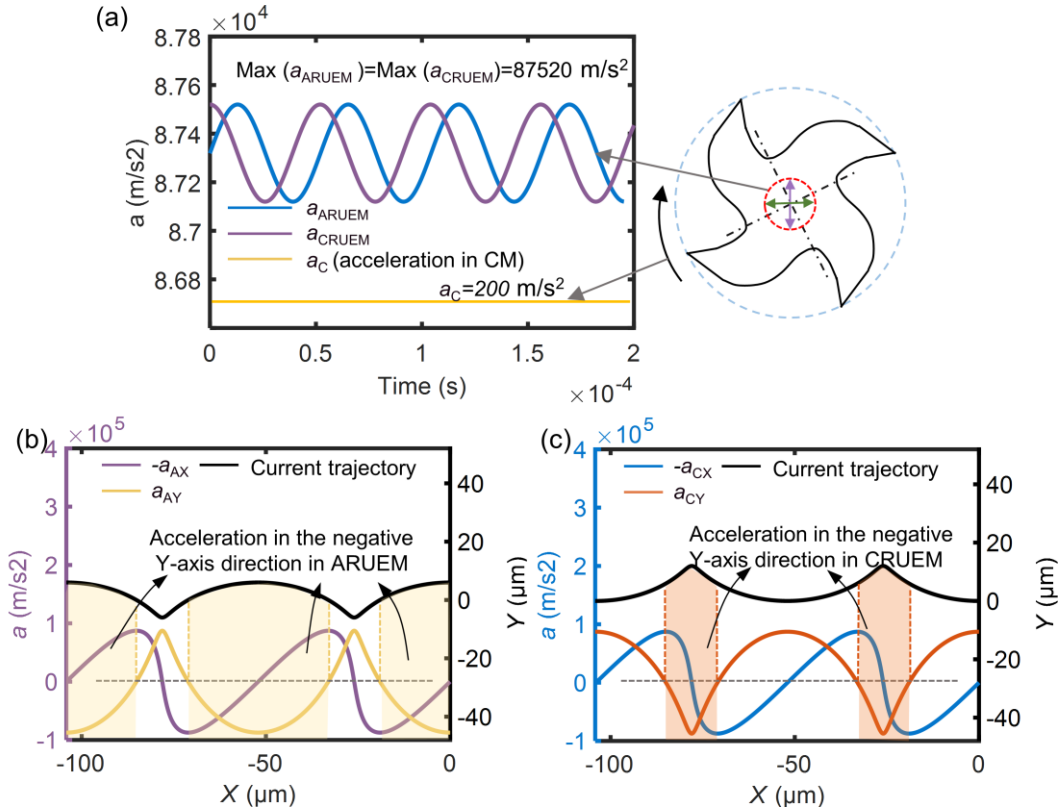

Fig. S2. Acceleration (a) varied with time, and varied with *X* position in (b) CRUEM and in (c) ARUEM at v_c = 60 m/min, A = 6 μm and v_f = 0.015 mm

S4: Corrected motion trajectory in ARUEM

The instantaneous working relief angle of cutting edges during the cutting process can be calculated based on the actual nominal relief angle α_0 through

$$\alpha=\alpha_0-\eta=\alpha_0-\arctan\left(\frac{v_y}{v_x}\right)\Big/\pi\times180. \tag{S11}$$

The instantaneous direction angle η of the cutting edge in ARUEM is defined as

$$\eta=\arctan\left(\frac{v_{AY}}{v_{AX}}\right)=\frac{60fA\sin(2\pi ft)}{nr+60fA\cos(2\pi ft)}. \tag{S12}$$

It can be calculated that the ironing phenomenon in ARUEM will not occur when the following

inequality has no solution.

$$\sqrt{\tan^2\alpha_0+1}\sin\left(2\pi ft-\arccos\left(\frac{1}{\sqrt{\tan^2\alpha_0+1}}\right)\right)>\frac{nr\tan\alpha_0}{60fA}. \tag{S13}$$

The above inequality can be further derived to obtain

$$\frac{nr\tan\alpha_0}{60fa\sqrt{\tan^2\alpha_0+1}}\geq 1. \tag{S14}$$

In CRUEM, the ironing phenomenon between the tool flank and the workpiece appears when $\alpha<0$ (Liu et al., 2023). And the conditions for the occurrence of the plastic extrusion phenomenon in CRUEM are the same as those in ARUEM. After verification, it was found that when the cutting speed is between 30 m/min and 90 m/min, and the vibration amplitude is between 4 μm and 8 μm, the conditions for the occurrence of the ironing phenomenon are met.

In ARUEM, the cutting tools begin to move along the tool flank when the instantaneous movement direction of the tool is parallel to the tool flank as $\eta=\alpha_0$. This time was recorded as t_1, and the starting points of the slip were recorded as (x_{t1}, y_{t1}) within one vibration cycle. Therefore, the trajectory of the cutting edge along the tool flank can be calculated as follows:

$$\frac{y-y_{t1}}{x-x_{t1}}=\tan\alpha_0. \tag{S15}$$

The movement along the tool flank terminates when it intersects with the free-state trajectory; the coordinates are (x_{t2} y_{t2}), and the time is t_2.

The corrected motion trajectory in the ARUEM can be expressed as

$$\begin{cases} x_A=-\dfrac{2\pi nr}{60}t-A\sin(2\pi ft) & 0\leq t\leq 1/f \\ y_A=A\cos(2\pi ft) & 0\leq t\leq t_1, t_2\leq t\leq 1/f \\ y_A=\left(x_{t2}-x_{t1}\right)\tan\alpha_0+y_{t1} & t_1<t<t_2 \end{cases}. \tag{S16}$$

Some situations need further clarification. The theoretical trajectory of the tool tip undergoes a reverse movement when the instantaneous vibration speed is greater than the linear speed of rotation of the milling cutter. The conditions for reverse motion can be calculated as follows:

$$\frac{2\pi nr}{60}\leq 2\pi fA. \tag{S17}$$

However, the trajectory of cutting edge moves along the tool flank is higher than the reverse motion area in the theoretical trajectory when the cutting speed is between 30 to 90 m/min and the vibration amplitude is between 4 to 8 μm. Therefore, the actual movement trajectory in the ARUEM, as mentioned above, is applicable within the range of the experimental parameters.

S5: Envelope curves of actual motion trajectory

Considering that the cutting edge has a blunt circular shape, it is simplified as a circle with a certain blunt radius. The envelope curves formed by the blunt edge under ARUEM and CRUEM are shown in Fig. S3. When the plastic and elastic deformations during the cutting process are not considered, the lower boundary of the envelope curve in Fig. S3 represents the cutting topography formed by the cutting edge. The residual height of a cutting edge in ARUEM was lower than that in CRUEM.

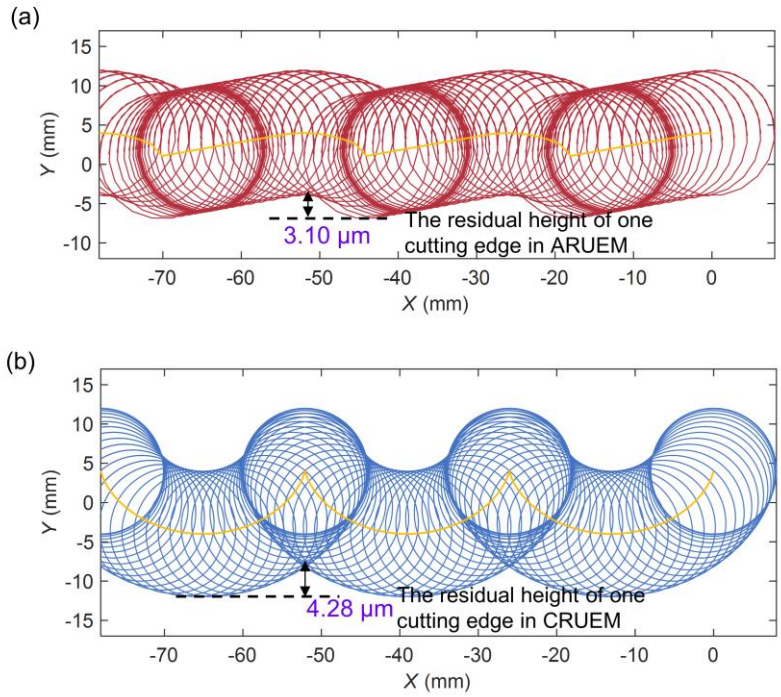

Fig. S3. Envelope curves of actual motion trajectory in: (a) ARUEM and (b) CRUEM considering rounded cutting edge with radius of 8 μm at v_c= 30 m/min, A=4 μm and v_f = 0.015 mm

S6: Ironing process in ARUEM and CRUEM

Fig. S4 illustrates a schematic diagram of the stress distribution of the ridge in ARUEM and CRUEM under the action of the cutting-edge ironing force. If the stress exceeds the yield strength of the material, plastic deformation occurs in the area, and the deformation will recover if the stress is lower than the yield strength. Since the maximum speed of the cutting edge is the same, it can be assumed that the mechanical energy of the cutting edges in ARUEM and CRUEM is similar. During the process of the cutting edge ironing the residual ridges, the mechanical energy of the cutting edge will be absorbed by the plastic deformation of the ridges. Additionally, the ridges in ARUEM are smoother, while the ridges in CRUEM are sharper. Therefore, the degree of plastic deformation in ARUEM is considerably smaller.

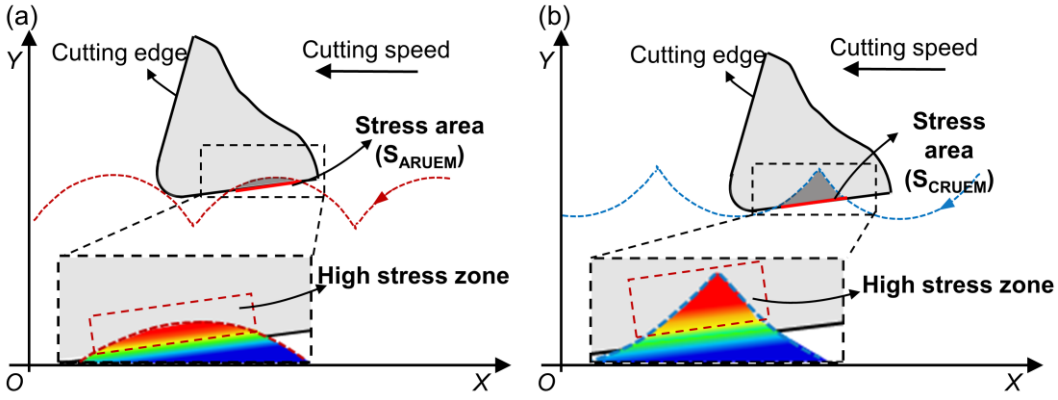

Fig. S4. Schematic of stress and strain of the ridge in (a) ARUEM and (b) CRUEM

S7: Rotary ultrasonic vibration cutting system

The dual-channel ultrasonic signal generator was designed in our laboratory and can generate two channels of ultrasonic signals with the same frequency and a phase difference of 90 °. The power of these two channels can be adjusted independently. The ultrasonic vibration transducer, also designed by our laboratory, consists of two sets of piezoelectric ceramic plates, an ultrasonic vibration transformer, a rear cover plate, and a carbide milling cutter, which is a part of the vibration transformer. The two sets of piezoelectric ceramic plates convert the electrical signals received from the dual-channel signal generator into bending vibrations with the same frequency and a 90 °phase difference, which are perpendicular to each other. The vibration is transmitted and amplified by the vibration amplitude transformer, ultimately generating elliptical vibration of the milling cutter on the plane perpendicular to the axial direction.

S8: Three-dimensional surface topography

The 3D topographies of the machined surfaces generated by different parameters are displayed in Fig. S5, from which the overall topographical characteristics are presented. The 3D topographies machined by CM are relatively flat, with some undulations at the macro level. These undulations are more pronounced at higher cutting speeds, indicating that the stability of the cutting process decreases as the cutting speed increases (Li et al., 2024). In contrast, uniform small patterns and flatter machined surfaces are observed in ARUEM and CRUEM. This is attributed to the high-frequency vibration of the milling cutter. Notably, a flatter surface with lower ridge and undulations heights was generated in ARUEM compared to CRUEM, indicating better cutting ability during ARUEM, which may be attributed to the unique cutting trajectory and the characteristics of speed and acceleration in ARUEM (Bai et al., 2024).

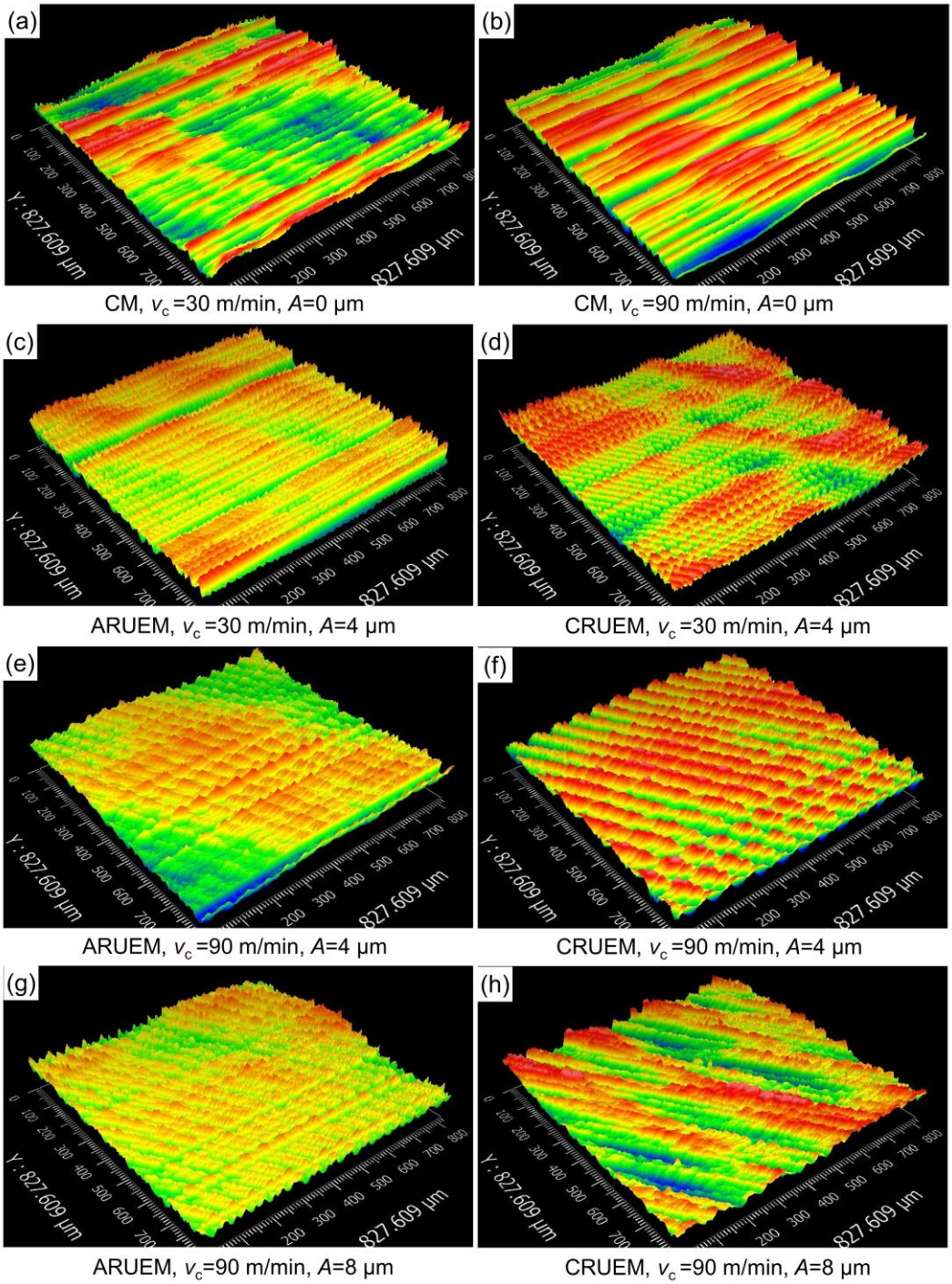

Fig. S5. Three-dimensional surface topography of Ti-6Al-4V machined using different milling parameters

References

Bai Q, Wang P, Cheng K, et al., 2024. Machining dynamics and chatters in micro-milling: A critical review on the state-of-the-art and future perspectives. *Chinese Journal of Aeronautics*, 37(7):59-80. https://doi.org/10.1016/j.cja.2024.02.022

Li Z, Song Q, Jin P, et al., 2024. Chatter suppression techniques in milling processes: A state of the art review. *Chinese Journal of Aeronautics*, 37(7):1-23. https://doi.org/10.1016/j.cja.2023.10.001

Liu JJ, Jiang XG, Han X, et al., 2019. Influence of parameter matching on performance of high-speed rotary ultrasonic elliptical vibration-assisted machining for side milling of titanium alloys. *International Journal Of Advanced Manufacturing Technology*, 101(5-8):1333-1348. https://doi.org/10.1007/s00170-018-3006-6

Liu Y, Geng D, Zhang D, et al., 2023. Cutting performance and surface integrity for rotary ultrasonic elliptical milling of inconel 718 with the ball end milling cutter. *Journal of Materials Processing Technology*, 319 https://doi.org/10.1016/j.jmatprotec.2023.118094

Sun Z, Geng D, Guo H, et al., 2024. Introducing transversal vibration in twist drilling: Material removal mechanisms and surface integrity. *Journal of Materials Processing Technology*, 325 https://doi.org/10.1016/j.jmatprotec.2024.118296